Combined Defect and Heterojunction Engineering in ZnTe/$CoTe_2$@NC Sulfur Hosts toward Robust Lithium-Sulfur Batteries

Chen Huang, Jing Yu, Canhuang Li, Zhibiao Cui, Chaoqi Zhang, Chaoyue Zhang*, Bingfei Nan, Junshan Li, Jordi Arbiol, and Andreu Cabot**

C. Huang, J. Yu, C. H. Li, C. Q. Zhang, C. Y. Zhang, B. F. Nan, A. Cabot

Catalonia Institute for Energy Research-IREC

Sant Adrià de Besòs, Barcelona 08930, Spain

E-mail: acabot@irec.cat

C. Huang, C. H. Li

Department of Chemistry

Universitat de Barcelona 08028, Spain

J. Yu, J. Arbiol

Catalan Institute of Nanoscience and Nanotechnology (ICN2), CSIC and BIST, Campus UAB, Bellaterra, 08193 Barcelona, Catalonia, Spain.

Z.B.Cui

School of Chemistry, South China Normal University, Guangzhou 510006, PR China

C. Q. Zhang

College of Materials Science and Engineering, Fuzhou University

No.2, Xueyuan Road, Minhou County, Fuzhou City, Fujian Province

350108, China

E-mail:czhang@irec.cat

C. Y. Zhang

Key Laboratory for Magnetism and Magnetic Materials of the Ministry of Education &

School of Physical Science & Technology

Lanzhou University Lanzhou 730000, China

E-mail: chzhang@irec.cat

J. S. Li

Institute for Advanced Study

Chengdu University 610106, Chengdu, China

J. Arbiol and A. Cabot

ICREA Pg. Lluis Companys, 08010 Barcelona, Catalonia, Spain

** Corresponding authors*

Keywords

Transition metal telluride, tellurium vacancies, heterostructure, lithium-sulfur battery, lithium polysulfides.

Abstract

The lithium-sulfur battery (LSB) is a feasible candidate for the next generation of energy storage devices, but the shuttle effect of lithium polysulfides (LiPSs) and the poor electrical conductivity of sulfur and lithium sulfides limit their practical application. In this work, a sulfur host material based on nitrogen-doped carbon (NC) coated with small amount of a transition metal telluride (TMT) catalyst is proposed to overcome these limitations. The properties of the sulfur redox catalyst are tuned by adjusting the anion vacancy concentration and engineering a ZnTe/$CoTe_2$ heterostructures. Theoretical calculations and experimental data demonstrate that tellurium vacancies enhance the adsorption of LiPSs, while the formed

TMT/TMT and TMT/C heterostructures as well as the overall architecture of the composite simultaneously provide high Li^+ diffusion and fast electron transport. As a result, v-ZnTe/$CoTe_2$@NC/S sulfur cathodes show excellent initial capacities up to 1608 $mA \cdot h \cdot g^{-1}$ at 0.1C and stable cycling with an average capacity decay rate of 0.022% per cycle at 1C during 500 cycles. Even at a high sulfur loading of 5.4 $mg \cdot cm^{-2}$, a high capacity of 1273 $mA \cdot h \cdot g^{-1}$ at 0.1C is retained, and when reducing the electrolyte to 7.5 $\mu L \cdot mg^{-1}$, v-ZnTe/$CoTe_2$@NC/S still maintains a capacity of 890.8 $mA \cdot h \cdot g^{-1}$ after 100 cycles at 0.1C.

1. Introduction

Sulfur cathodes are regarded as a viable and advantageous alternative for the forthcoming generation of energy storage devices due to their high energy density (2600 Wh kg^{-1}) and specific capacity (1675 mAh g^{-1}) as well as the large sulfur abundance and low cost.[1] However, sulfur-related limitations such as the shutting of lithium polysulfides (LiPSs), poor conductivity of the charged and discharged cathode active material (S_8/Li_2S), inefficient sulfur usage, and huge volume expansion during charging and discharging restrain the practical application of lithium-sulfur batteries (LSBs).[2] To solve these shortcomings, various approaches have been considered, including the development of sulfur hosts[3] and the engineering of functional separators and binders able to trap the polysulfides.[4] Particularly, the use of catalytically-active sulfur hosts has been shown to accelerate sulfur reduction and oxidation reactions and has thus received considerable attention in recent years.[1a, 5]

While porous and high surface area carbon materials (e.g. graphene, carbon nanotubes, and carbon fibers) are frequently used as sulfur hosts,[6] the weak interaction between

nonpolar carbon materials and polar polysulfides is unable to inhibit the dissolution and shutting effect of LiPSs.[7] Nitrogen[8] and supplementary metal additives can be introduced to capture the LiPS and accelerate their conversion.[9]Transition metal compounds (oxides, phosphides, carbides, and chalcogenides) have been shown particularly effective as polar catalytic additives in sulfur cathodes.[10] Among them, transition metal tellurides (TMTs) have been systematically ignored due to their high density as well as the low abundance and high cost of tellurium. Nevertheless, TMTs offer several patent advantages over the wide variety of tested compounds that, if used in very small quantities, could help balance and potentially overcome their drawbacks. These advantages include (i) much higher electrical conductivities (e.g., 1.15 $\times 10^6$ S m^{-1} for $NiTe_2$) compared with oxides, sulfides, and selenides counterparts (e.g. 0.55 S m^{-1} for NiS_2), [11]and (ii) high catalytic activities related to the metal cation (Co^{2+}, Zn^{2+}, and Ni^{2+}) forming an octahedral complex with Te_2^{2-} in a low-spin state, while the metal 3d orbital splits into two subordinate orbitals, t_{2g} and e_g. In TMTs, the metal ions adopt different spin modes in the three-dimensional electronic configuration, which can promote the rapid charge transfer of the electrode and the LiPS conversion.[12]

To minimize the amount of TMT additive, suitable composite designs must be built, incorporating effective heterostructures and assuring a large TMT dispersion. Besides, given the close correlation between catalytic activity and electronic band structure, to optimize the electrocatalytic performance of the host, it is necessary to adjust the electronic properties of the active sites. At the material architecture level, these electronic properties can be adjusted through interface engineering. Additionally, at the atomic level, electronic characteristics can be tuned by regulating the coordination environment of the active site.

At the material architecture level, heterostructures composed of materials with different bandgaps have been widely used to optimize electronic parameters in electrode materials for photo/electrocatalysis,[13] batteries,[14] and supercapacitors.[15] At the interface of two different semiconductors, rich phase boundaries, charge accumulation/depletion, an electric field, and electronic band bending are encountered.[16] These singular regions can promote the diffusion of ions/electrons and thus accelerate the conversion reaction. For example, Zhang et. al prepared heterostructured Fe_3C-FeN nanoparticles in a three-dimensional-ordered nitrogen-doped carbon and demonstrated the Fe_3C/FeN heterointerface to exhibit high sulfiphilicity. [17]

At the atomic level, vacancy engineering, particularly anionic vacancies, has been demonstrated as a successful approach to significantly improve material properties by just modifying the compound stoichiometry.[15d, 18]Within sulfur hosts for LSB cathodes, introducing an anion vacancy not only generally increases the number of carriers within the crystal and changes the electronic structure near the defect sites, but the activated unpaired cations can also capture polysulfides efficiently,[19] thus improving the sulfur utilization rate. As an example in this direction, Wang et al. used an acid etching approach to produce ZnS nanotubes with abundant sulfur vacancies, which they then supported on freestanding carbon cloth to use as LSB electrode. They showed the combination of architectural and sulfur-vacancy engineering to effectively modulate the electronic structure of ZnS, enhance its interactions with active sulfur, facilitate ion/electron transfer, and ultimately improve the LSB performance.[19b] Numerous other previous works have explored the effects of oxygen and sulfur vacancies on the performance of LSBs, however, the chemical affinity and catalytic activity of Te vacancies as LiPSs have been very rarely considered.[11b, 20]

Defect and heterojunction engineering strategies have been validated separately in the context of LSBs, but no catalysts that simultaneously use both of these two electronic modification strategies to test their compatibility and potential synergy have been reported. Given the intricate nature of the Li-S reaction system, a single approach is unlikely to effectively meet the multiple challenges posed by LSBs.

The present study employs a dual engineering approach, manipulating vacancies and heterointerfaces, to develop an optimized TMT-based catalytic additive. More precisely, N-doped carbon-coated bimetallic telluride heterostructures containing Te vacancies (v-ZnTe/$CoTe_2$@NC) are used as sulfur hosts in LSBs. We showcase here the exceptional specific capacity, stable cycling, and superior rate capability of v-ZnTe/$CoTe_2$@NC as sulfur host, which can be attributed to the synergistic effects and functionality of vacancies and heterointerface. These effects are observed even at high loading and in lean electrolyte conditions, thereby highlighting the remarkable potential of this system.

2. Results and discussions

Scheme 1a illustrates the synthesis steps used to prepare v-ZnTe/$CoTe_2$@NC/S cathode materials and **Scheme 1b** the conversion between S_8 and Li_2S involved in the LSB charging and discharging process. The synthesis details can be found in the **Supporting Information** (SI). Briefly, first, a zeolitic imidazole framework (ZIF), particularly the zinc-based ZIF-8, was synthesized by a self-assembly method at room temperature.[21] Afterward, a second metal-organic framework (MOF), cobalt-based ZIF-67, with the same crystal structure as ZIF-8, was coprecipitated on the surface of the preformed ZIF-8 to produce ZIF-8/ZIF-67 core-shell structures.[22] Afterward, ZIF-8/ZIF-67 particles were uniformly coated with

polydopamine (PDA) using a tris-buffer solution (ZIF-8/ZIF-67@PDA). Then, tellurium powder was reacted at 600 ºC with the Co and Zn cationic nodes of the ZIF-8/ZIF-67@PDA precursor to obtain a zinc telluride/cobalt telluride heterostructure. Meanwhile, PDA organic molecules shrank to form a porous structure and were carbonized to form N-doped carbon (NC). Subsequently, Te vacancies were generated by annealing ZnTe/$CoTe_2$@NC under a reducing atmosphere (Ar/H_2). Finally, the sulfur-containing v-ZnTe/$CoTe_2$@NC/S composite was produced using a melt-infiltration process.

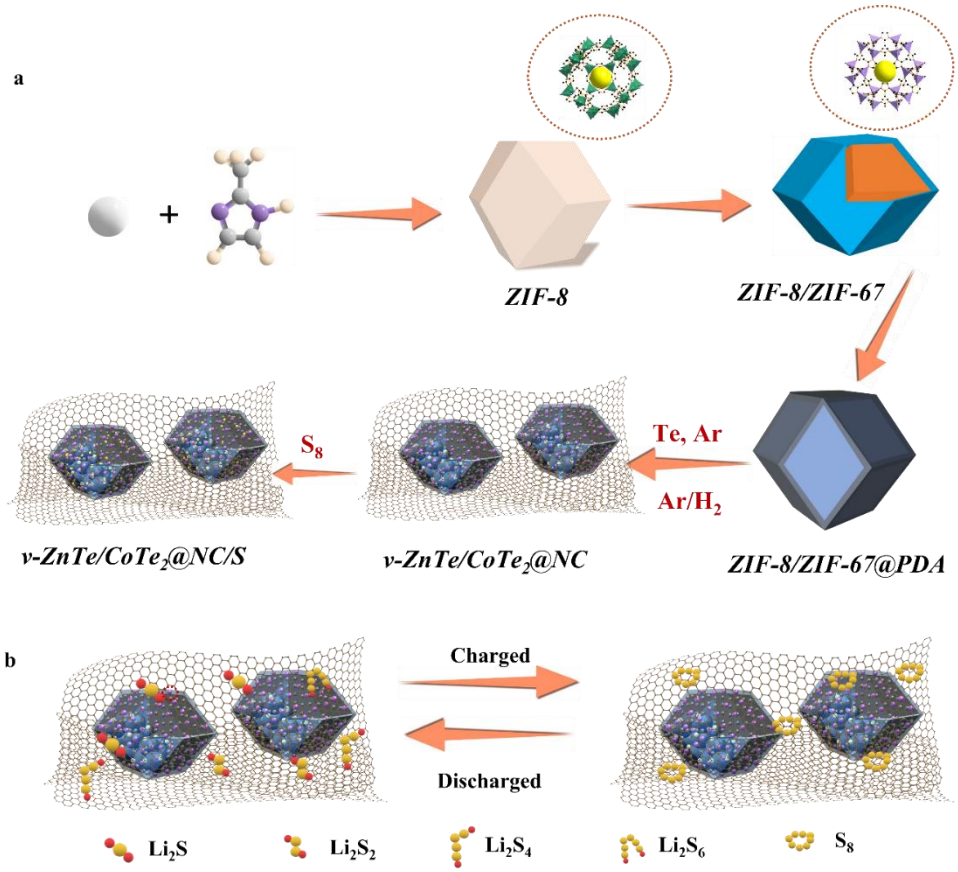

Scheme 1. (a) Schematic illustration of the synthesis procedure used to produce v-ZnTe/$CoTe_2$@NC/S composites. (b) Scheme of the LSB charging and discharging process.

The morphology of the as-prepared electrode materials was monitored by scanning electron microscopy (SEM) and transmission electron microscopy (TEM). Representative

SEM images of the precursor are shown in **Figures 1a and S1**. ZIF-8, ZIF-8/ZIF-67, and ZIF-8/ZIF-67@PDA all show the conventional dodecahedral particle morphology with a regular and smooth surface. [21b, 22b, 23] Due to the growth/coating of the additional layer, the ZIF-8/ZIF-67@PDA particle size is larger than that of ZIF-8, at 550 nm and 500 nm respectively. ZnTe/$CoTe_2$@NC obtained by reacting ZIF-8/ZIF-67@PDA with Te inherited the dodecahedral particle morphology (**Figure 1b**). However, the pyrolysis process resulted in a notable agglomeration and shrinkage of the ZnTe/$CoTe_2$@NC particles, down to 200 nm. After annealing under a reducing atmosphere to generate Te vacancies, the produced v-ZnTe/$CoTe_2$@NC material maintained the aggregation, particle size, and morphology of ZnTe/$CoTe_2$@NC (**Figure 1c**). Representative TEM images of the final sulfur host material, v-ZnTe/$CoTe_2$@NC, are shown in **Figures 1d and S2**. v-ZnTe/$CoTe_2$@NC is formed by ca. 200 nm hollow polycrystalline particles with a crystal domain size of about 10 nm. Electron energy loss spectroscopy (EELS) chemical composition maps display an uneven distribution of N, Te, Zn, Co, C within the v-ZnTe/$CoTe_2$@NC nanostructured dodecahedral particles (**Figure 1e and S3**). We observe multiple nanodomains of ZnTe and $CoTe_2$, while N is mainly distributed on the material surface provided by the initial PDA coating. Results from the SEM-energy dispersive x-ray spectroscopy (EDX) spectra of ZnTe/$CoTe_2$@NC, v-ZnTe/$CoTe_2$@NC and the reference $CoTe_2$@NC and ZnTe@NC materials are displayed in **Figure S4**. EDX analysis shows the amount of Te in v-ZnTe/$CoTe_2$@NC to be ca. 10% lower than in ZnTe/$CoTe_2$@NC (**Figure S4**).

The high-resolution TEM (HRTEM) image of v-ZnTe/$CoTe_2$@NC in **Figure 1f** shows that the lattice fringes displayed in the red squared magnified detail correspond to the (022),

(210), and (2-1-2) crystal planes of ZnTe visualized along the [1-22] zone axis, while the lattice spacings shown in the orange squared detail correspond to the (220) and (1-20) crystal planes of $CoTe_2$ visualized along its [001] zone axis. In addition, a distinct ZnTe/$CoTe_2$ interface can be observed in **Figure 1g**.

The XRD patterns of v-ZnTe/$CoTe_2$@NC and ZnTe/$CoTe_2$@NC show the fingerprints of both the cubic ZnTe phase (F-43m, peaks at 25.3°(111), 41.8°(220), and 49.5°(311), JCPDS PDF#15-0746), and the orthorhombic phase of $CoTe_2$ (Pnn2, peaks at 31.7°(111), 32.9°(120), 43.5°(211), JCPDS PDF#89-2091) as shown in **Figure 2a**.[24] The absence of discernible XRD peaks from the carbon shell is ascribed to the strong crystallinity of the metal tellurides (ZnTe/$CoTe_2$). To analyze the graphitization degree of carbon, we compared the intensities of the D (1350 cm^{-1}) and G (1590 cm^{-1}) Raman vibrational modes associated with the disordered structure and bond stretching motion of sp^2 hybridized carbon, respectively (**Figure S5 and Table S1**).[25] While amorphous carbon provides more electrochemically active sites, graphitized carbon improves catalyst conductivity and promotes charge transfer. However, no significant variations were observed among the various samples. The I_D/I_G peak intensity ratio was less than 1 in all the carbon-containing samples (v-ZnTe/$CoTe_2$@NC, ZnTe/$CoTe_2$@NC, $CoTe_2$@NC, and ZnTe@NC), indicating that the carbonization process was highly effective in forming graphitized carbon from PDA.

The specific surface area and pore volume of v-ZnTe/$CoTe_2$@NC, ZnTe/$CoTe_2$@NC, $CoTe_2$@NC, and ZnTe@NC were investigated using N_2 adsorption/desorption isotherms (**Figure S6a**). The Brunauer-Emmett-Teller (BET) specific surface area of v-ZnTe/$CoTe_2$@NC, ZnTe/$CoTe_2$@NC, $CoTe_2$@NC, and ZnTe@NC was 589 m^2 g^{-1}, 537.2 m^2

g^{-1}, 518.9 m^2 g^{-1} and 485.6 m^2 g^{-1}. In addition, the pore sizes of the four sulfur host cathode materials were concentrated in the range of 0-50 nm (**Figure S6b**). The huge specific surface areas and small pores characterizing the produced materials are suitable to accommodate and disperse sulfur, preventing the dissolution and shuttling of sulfur during the electrochemical reaction, and further improving the utilization of active materials.[1c]

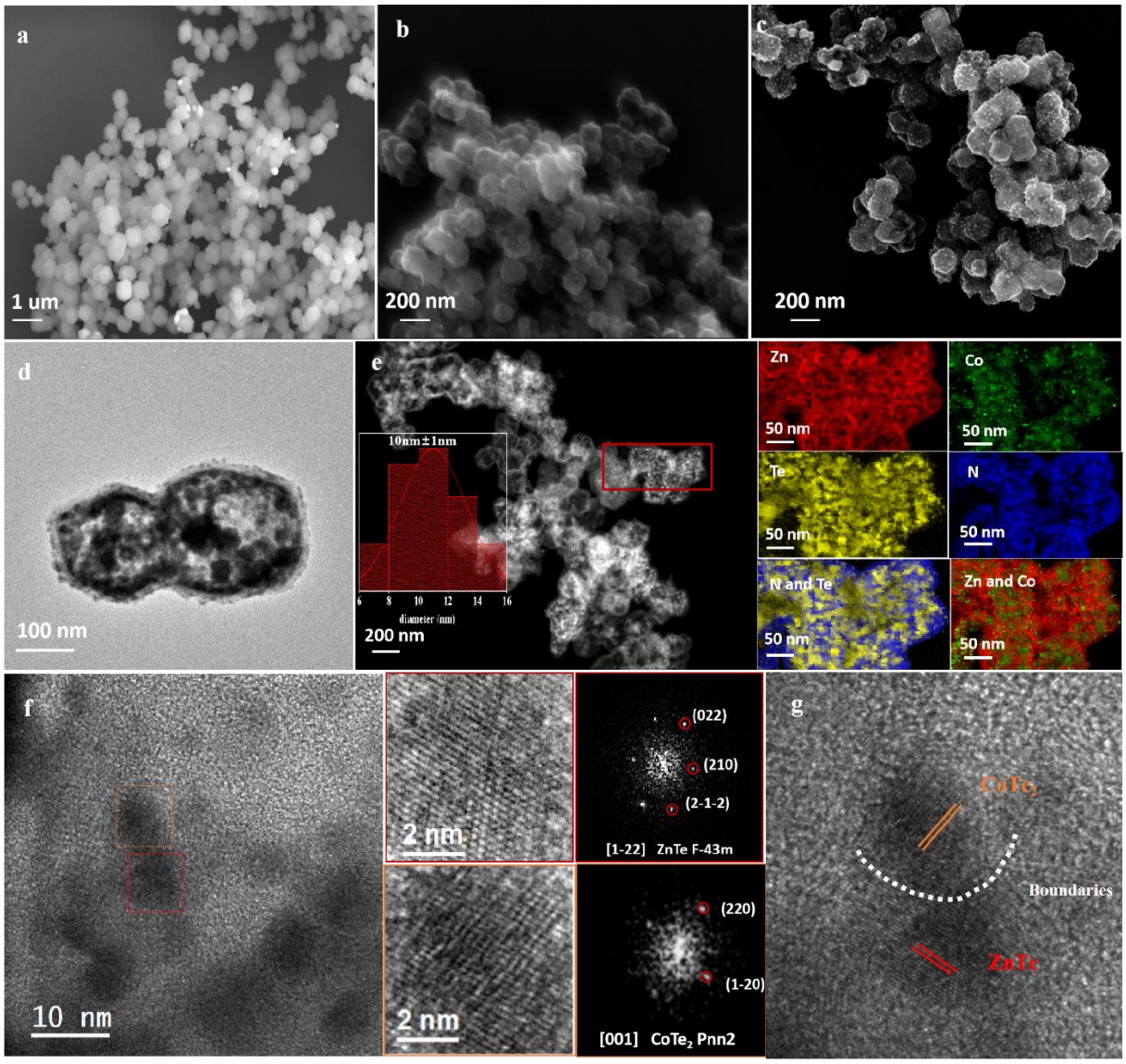

Figure 1. (a-c) SEM images of ZIF-8/ZIF-67@PDA, ZnTe/$CoTe_2$@NC, and v-ZnTe/$CoTe_2$@NC. (d) Low-magnification HAADF-STEM image of v-ZnTe/$CoTe_2$@NC. (e)

EELS chemical composition maps of v-ZnTe/$CoTe_2$@NC obtained from the red squared area in the STEM micrograph. (f-g) HRTEM micrographs from the v-ZnTe/$CoTe_2$@NC sample showing ZnTe and $CoTe_2$ crystal domains and a ZnTe/$CoTe_2$ interphase, and their corresponding power spectrum.

While no significant electron paramagnetic resonance (EPR) peak was obtained from ZnTe/$CoTe_2$@NC, the v-ZnTe/$CoTe_2$@NC sample displayed a sharp signal at g=2.003 that can be assigned to the existence of unpaired electrons and associated with the Te vacancies generated during the thermal process under reducing (Ar/H_2) atmosphere (**Figure 2b**).

The Co 2p X-ray photoelectron spectroscopy (XPS) spectrum of ZnTe/$CoTe_2$@NC displays one doublet assigned to Co^{2+} at 780.7 eV (Co $2p_{3/2}$) and 796.4 eV (Co $2p_{1/2}$) (**Figure 2c**). These binding energies are redshifted compared with $CoTe_2$@NC (781.0 eV and 796.7 eV), [24] indicating an electronic influence of the ZnTe within the ZnTe/$CoTe_2$@NC. The Zn 2p XPS spectrum also displays a doublet at 1021.6 eV (Zn $2p_{3/2}$) and 1044.7 eV (Zn $2p_{1/2}$) assigned to Zn^{2+} (**Figure 2d**). This doublet is blueshifted with respect to ZnTe@NC. [26] The simultaneous blueshift of the Zn 2p spectrum and redshift of the Co 2p spectrum in ZnTe/$CoTe_2$@NC points towards a decrease in the electronic density of Zn^{2+} within ZnTe and an increase in Co^{2+} within $CoTe_2$, which is consistent with an electronic injection from ZnTe to $CoTe_2$. The Te 3d XPS spectra show two doublets at 572.3eV/583.1 eV and 575.2eV/586.1 eV assigned with metal-Te bonds and tellurium oxide formed by surface oxidation of the ZnTe/$CoTe_2$ (**Figure 2e**).[24] A slight positive shift of the binding energy is also observed for the Te^{2-} component of $CoTe_2$@NC compared with $ZnTe_2$@NC, while the Te 3d spectrum of the ZnTe/$CoTe_2$@NC appears in between those of $CoTe_2$@NC and

$ZnTe_2$@NC. Compared with ZnTe/$CoTe_2$@NC, the Co 2p, Zn 2p and Te 3d XPS spectra of v-ZnTe/$CoTe_2$@NC are negatively shifted. This is consistent with the presence of Te vacancies increasing the electronic density at anionic sites.[19a] The C1s XPS spectra display peaks at 284.6, 286.2, and 288.4 eV attributed to C=C, C-O, and C=O respectively (**Figure S7a**).[1c] The N 1s spectra show strong bands demonstrating the presence of N within the carbon (**Figure S7b**). Three peaks at binding energies of 398.4, 399.8, and 402.1eV, corresponding to pyridinic-N, pyrrolic-N, and graphitic-N were fitted. According to previous reports, N, especially pyridinic-N, can efficiently increase electron density and interaction with sulfur/polysulfides. It was also reported that the pyridinic-N and pyrrolic -N could effectively improve the affinity and binding energy of polar atoms with elemental sulfur (S_8) and polar polysulfides (Li_2S_n, $4 \leq n \leq 8$) by the strong Lewis acid-base interaction.[27]

Four-point probe conductivity tests (**Figure 2f**) showed v-ZnTe/$CoTe_2$@NC to have a slightly higher electrical conductivity, 7.2×10^2 S cm^{-1}, than ZnTe/$CoTe_2$@NC (6.4×10^2 S cm^{-1}), $CoTe_2$@NC (3.5×10^2 S cm^{-1}), and ZnTe@NC (1.8×10^2 S cm^{-1}). The moderate electrical conductivity differences are related to the dominant role played by NC in the charge transport properties of the overall layer. Still, the larger conductivities obtained for v-ZnTe/$CoTe_2$@NC are explained by the additional carriers contributed by the presence of vacancies. Besides, both heterostructured materials, v-ZnTe/$CoTe_2$@NC and ZnTe/$CoTe_2$@NC, show much larger electrical conductivities than the single telluride materials, ZnTe@NC and $CoTe_2$@NC, which demonstrate the formed heterostructure to significantly contribute to improving charge transport.

DFT calculations were used to gain insight into the heterostructure electronic properties and effects (**Figure 2g**). DFT calculations of the total density of states (TDOS) of ZnTe were able to reproduce the discontinuous bandgap at the Fermi level providing the semiconductor behavior. In contrast, we found the conduction band of ZnTe/$CoTe_2$ contains prominent hybridization bands that introduce a large TDOS at the Fermi level. While the TDOS of both v-ZnTe/$CoTe_2$ and ZnTe/$CoTe_2$ are continuous, the d band center of the two materials is compared by PDOS, showing that the d band center of the heterostructure electrode material with Te vacancies is slightly closer to the Fermi level. According to d-band theory, the shift of the d-band center of a metal toward the Fermi level increases the probability of electrons filling the antibonding orbital between the metal and adsorbed molecules, which boosts the ability to adsorb sulfur species.[28] Therefore, for v-ZnTe/$CoTe_2$@NC, the d-band shift caused by vacancies is expected to enhance the adsorption capacity of LiPSs and promote the deposition of Li_2S in subsequent battery tests.

DFT calculations of a theoretical slab model based on ZnTe and $CoTe_2$ were used to determine the electron gain and loss of atoms near the contact interface (see details in the Supporting Information). As shown in **Figure 2h-i**, the differential charge distribution demonstrates that electron transfer occurs at the heterointerface between ZnTe and $CoTe_2$. To quantitatively determine the charge redistribution at the v-ZnTe/$CoTe_2$ interface and quantify the electron transfer between different atoms at the interface, a Bader charge analysis was performed (**Figure 2j-k**). From the Bader charge analysis, the acquisition of 1.26 electrons by the $CoTe_2$ unit from the ZnTe layer was calculated for v-ZnTe/$CoTe_2$. On the other hand, for ZnTe/$CoTe_2$, the $CoTe_2$ unit obtains 0.39 electrons from the ZnTe layer. Thus, in v-

ZnTe/$CoTe_2$ the $CoTe_2$ obtains a significantly large amount of charge (0.87 additional electrons) from the ZnTe layer, than in ZnTe/$CoTe_2$, indicating that vacancies have a very strong effect on the interphase charge redistribution. The gain of electrons by $CoTe_2$ coming from ZnTe is consistent with XPS results.

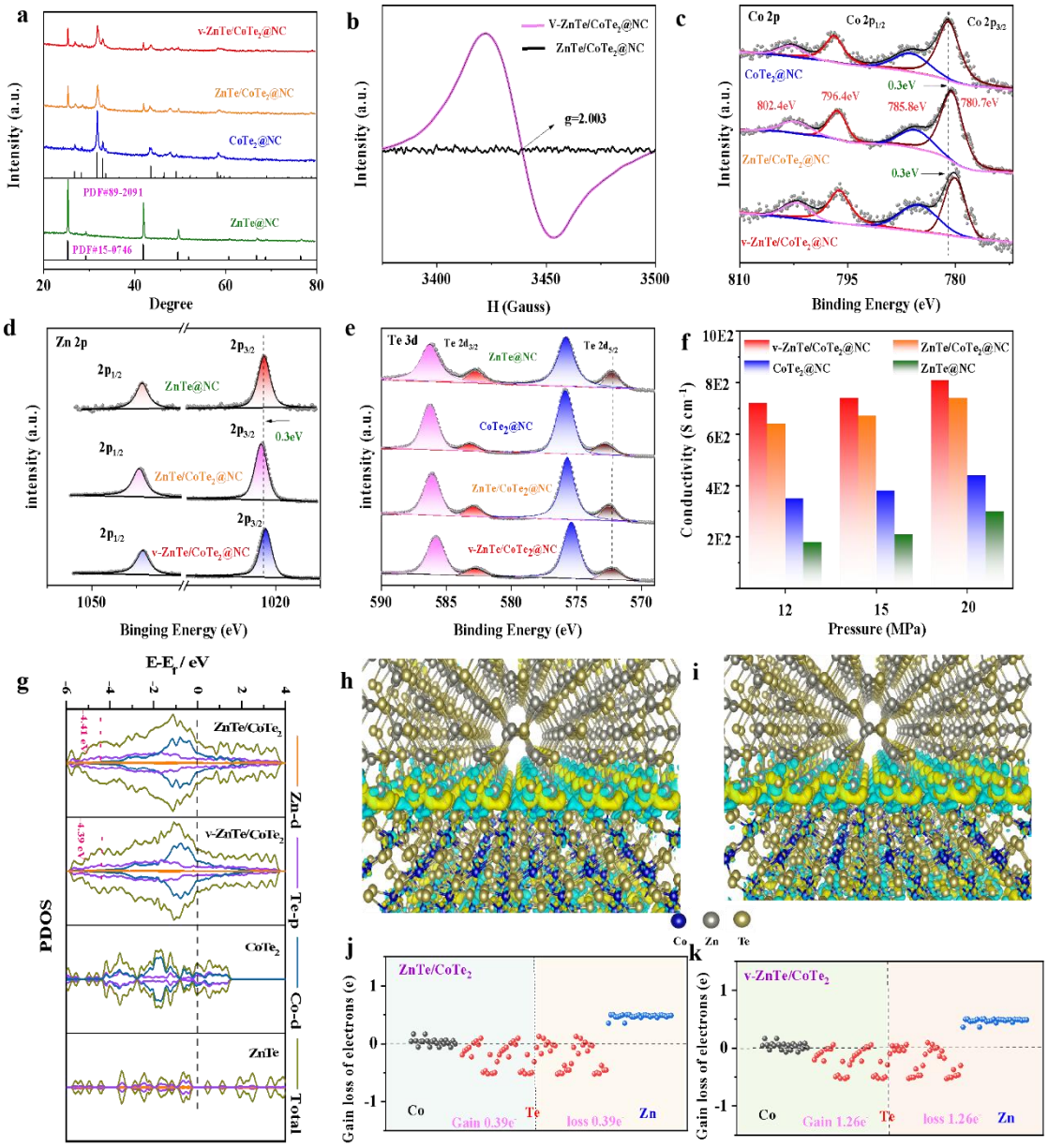

Figure 2 (a) XRD patterns of v-ZnTe/$CoTe_2$@NC, ZnTe/$CoTe_2$@NC, $CoTe_2$@NC, and ZnTe@NC. (b) EPR images of the v-ZnTe/$CoTe_2$@NC and ZnTe/$CoTe_2$@NC. (c) XPS Co

2p core-level spectrum. (d) Zn 2p core-level spectrum. (e) Te 3d core-level spectrum. (f) Electrical conductivity of v-ZnTe/$CoTe_2$@NC, ZnTe/$CoTe_2$@NC, $CoTe_2$@NC, and ZnTe@NC tested by the four-point probe method at different pressures. (g) Density of states (DOS) of v-ZnTe/$CoTe_2$, ZnTe/$CoTe_2$, $CoTe_2$, and ZnTe. The d band center is marked with a blue dotted line. (h-k) Electron gain/loss of different atoms calculated by Bader charge analysis. In panels h and I, yellow represents the gain of electrons and blue represents the loss of electrons.

Li_2S_6 adsorption experiments were performed to determine the LiPS adsorption ability of the different compounds. Equal amounts of v-ZnTe/$CoTe_2$@NC, ZnTe/$CoTe_2$@NC, $CoTe_2$@NC, and ZnTe@NC were introduced into 8 mM Li_2S_6 solutions and left undisturbed overnight (see details in the SI). As observed from the optical images shown in **Figure 3a**, while the initial Li_2S_6 solution was dark brown, after overnight absorption, the supernatant of the solution containing ZnTe/$CoTe_2$@NC shows a significantly lighter color than that of the solutions containing ZnTe@NC and $CoTe_2$@NC, indicating that the formation of heterostructures is beneficial to the adsorption of polysulfides. Besides, the supernatant of the solution containing v-ZnTe/$CoTe_2$@NC was even more decolored, demonstrating that v-ZnTe/$CoTe_2$@NC has an even stronger affinity towards Li_2S_6, which must be associated with the presence of Te vacancies. The LiPS adsorption was further analyzed by UV-vis spectroscopy (**Figure 3b**), Li_2S_6 shows an obvious absorption band in the range of 350 nm - 400 nm, which gradually decreases in the presence of adsorbent materials. Particularly, no UV-vis absorption peak is observed in the solution containing v-ZnTe/$CoTe_2$@NC.

After the LiPSs adsorption tests, v-ZnTe/$CoTe_2$@NC was dried and characterized by XPS (**Figure 3c-d**). The high-resolution Co 2p and Zn 2p spectra of the sample after LiPS adsorption appeared slightly shifted toward lower binding energies compared with fresh v-ZnTe/$CoTe_2$@NC. This shift is attributed to the Co/Zn active sites chemically bonding with the more electronegative S atoms in LiPSs.

DFT calculations were performed to further analyze the interaction between host materials and LiPSs. The surface adsorption configuration of six different sulfur-containing species (Li_2S, Li_2S_2, Li_2S_4, Li_2S_6, Li_2S_8, and S_8) in v-ZnTe/$CoTe_2$ and ZnTe/$CoTe_2$ were optimized as shown in **Figures S8 and S9.** DFT results show that the LiPSs binding energy of v-ZnTe/$CoTe_2$ is higher than that of ZnTe/$CoTe_2$ at the six stages of the lithiation process. **Figure 3e-f** shows the Li_2S_6 adsorption configuration on v-ZnTe/$CoTe_2$ and ZnTe/$CoTe_2$. The adsorption energies of Li_2S_6 on the surfaces of v-ZnTe/$CoTe_2$ and ZnTe/$CoTe_2$ are −1.37 and −1.31 eV, respectively. The bond length of Li–S on the v-ZnTe/$CoTe_2$ (3.48 Å) is longer than on ZnTe/$CoTe_2$ (3.03 Å), which reveals that v-ZnTe/$CoTe_2$ can facilitate the decomposition of Li_2S. These results are consistent with Te vacancies within ZnTe/$CoTe_2$ effectively promoting the adsorption of polysulfides.

To evaluate the LiPSs conversion ability in the presence of different catalysts, symmetrical cells with different host materials in 0.5 M Li_2S_6 electrolyte were assembled and tested using cyclic voltammetry, CV, **Figure 3g**). Compared with ZnTe/$CoTe_2$@NC, $CoTe_2$@NC, and ZnTe@NC cells, the v-ZnTe/$CoTe_2$@NC symmetric cells show the highest current density, which points to an enhanced catalytic ability. Notice that the CV curve

obtained in a Li_2S_6-free electrolyte shows a low current response, which demonstrates that lithiation/delithiation reactions dominate the current response.

The kinetics of the Li_2S nucleation process on the surfaces of v-ZnTe/$CoTe_2$@NC, ZnTe/$CoTe_2$@NC, $CoTe_2$@NC, and ZnTe@NC were studied to evaluate the catalytic activity of the sulfur hosts. The v-ZnTe/$CoTe_2$@NC cathode exhibited faster nucleation time and higher current response in the potentionstatic test at 2.05 V compared to ZnTe/$CoTe_2$@NC, $CoTe_2$@NC and ZnTe@NC (**Figure 3h**). According to Farady's theory ($\boldsymbol{Q = It}$, where $\boldsymbol{Q}$, $\boldsymbol{I}$and $\boldsymbol{t}$ represent capacity, discharge current, and time respectively), the capacity of v-ZnTe/$CoTe_2$@NC is 238.4 mA h g^{-1}, which is much higher than that of ZnTe/$CoTe_2$@NC (201.7 mAh g^{-1}), $CoTe_2$@NC (182.6 mAh g^{-1}) and ZnTe@NC (147.8 mAh g^{-1}). Overall, these experimental results show that the v-ZnTe/$CoTe_2$@NC electrode can effectively reduce the Li-S redox reaction overpotential, restrain the LiPSs shuttle effect, and promote the nucleation reaction of Li_2S.

The Tafel curves of different sulfur host cathodes are shown in **Figure 3i**. Compared with ZnTe/$CoTe_2$@NC, $CoTe_2$@NC, and ZnTe@NC, v-ZnTe/$CoTe_2$@NC is characterized by the smallest Tafel slope, which further indicates that v-ZnTe/$CoTe_2$@NC can promote the formation of Li_2S and accelerate the oxidation reaction kinetics.

DFT calculations were further used to determine the Gibbs free energies of the v-ZnTe/$CoTe_2$ and ZnTe/$CoTe_2$ reduction pathways. The lithiation pathway for the Li_2S formation from S_8 was studied. The optimized model and free energy distribution of polysulfide intermediates are shown in **Figure 3j**. The first step is the reaction of two Li^+ with S_8 to form Li_2S_8. Subsequently, Li_2S_8 is further reduced to Li_2S_6, Li_2S_4, Li_2S_2, and finally,

Li_2S. For both v-ZnTe/$CoTe_2$ and ZnTe/$CoTe_2$, the maximum Gibbs free energy increase was obtained for the transformation of Li_2S_6 to Li_2S_4, being the Gibbs free energy change for the v-ZnTe/$CoTe_2$ sample lower than that of ZnTe/$CoTe_2$. This result shows that the reaction thermodynamics of S is more favorable on v-ZnTe/$CoTe_2$ than on ZnTe/$CoTe_2$.

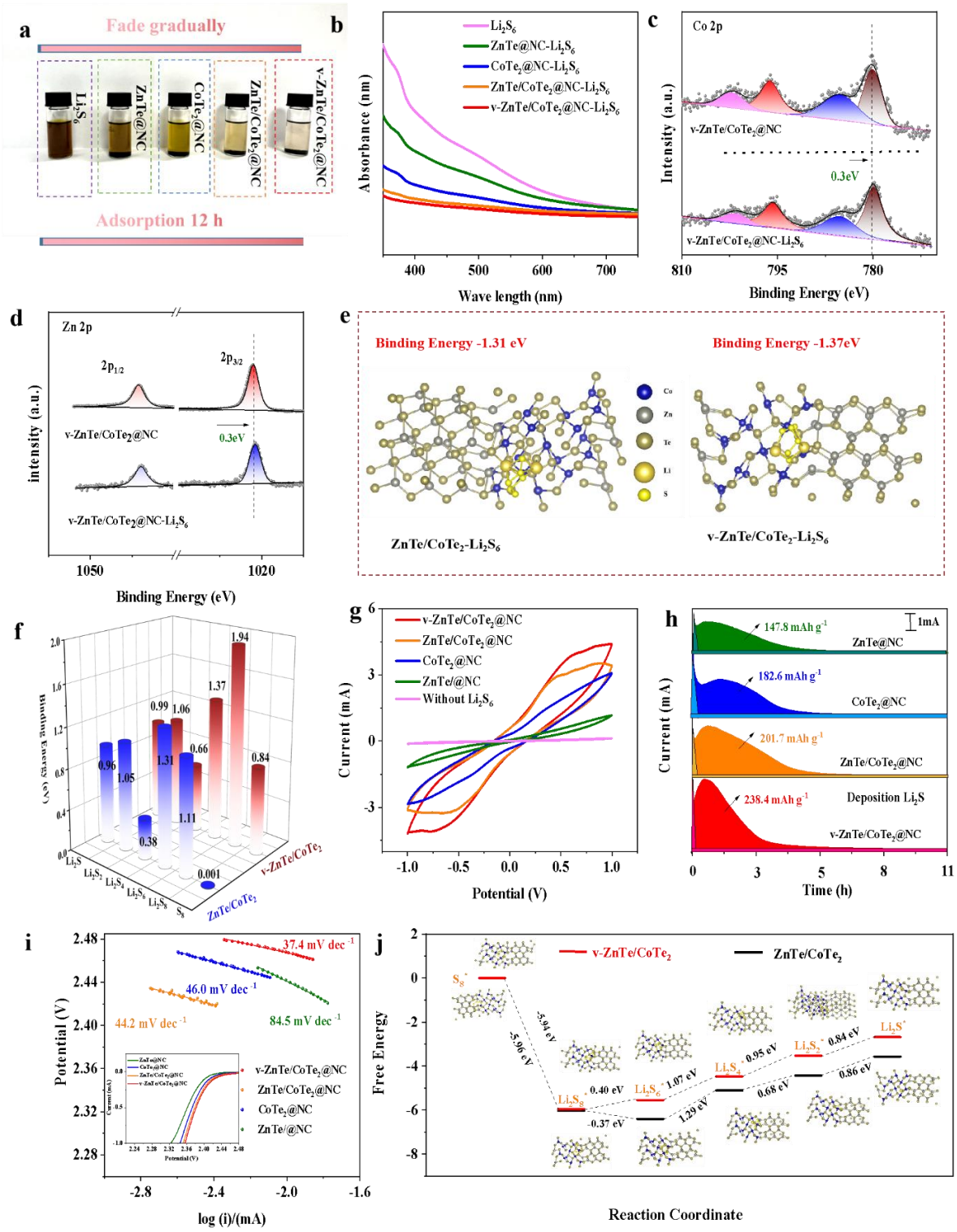

Figure 3 Photographs (a) and absorbance curves (b) of the static Li_2S_6 adsorption experiment. (c) Co 2p XPS spectra of v-ZnTe/$CoTe_2$@NC and v-ZnTe/$CoTe_2$@NC-Li_2S_6. (d) Zn 2p XPS spectra of v-ZnTe/$CoTe_2$@NC and v-ZnTe/$CoTe_2$@NC-Li_2S_6. (e) Model of the binding

energy to Li_2S_6 to v-ZnTe/$CoTe_2$ and ZnTe/CoTe. (f) Binding energies of different polysulfides (S_8, Li_2S_8, Li_2S_6, Li_2S_4, Li_2S_2 and Li_2S) to v-ZnTe/$CoTe_2$ and ZnTe/$CoTe_2$. (g) CV curves of symmetric cells with different electrode compositions (v-ZnTe/$CoTe_2$@NC, ZnTe/$CoTe_2$@NC, $CoTe_2$@NC, and ZnTe@NC) at the scan rate of 5 mVs^{-1}. (h) Potentiostatic discharge curves on different electrodes for studying the nucleation kinetics of Li_2S. (i) Tafel plots and LSV polarization curves (insert) of v-ZnTe/$CoTe_2$@NC, ZnTe/$CoTe_2$@NC, $CoTe_2$@NC, and ZnTe@NC (j) Gibbs free energy profiles and optimized adsorption model of LiPS species on v-ZnTe/$CoTe_2$ and ZnTe/$CoTe_2$.

To study the electrochemical performance of the different materials as sulfur hosts, they were infiltrated with S to obtain v-ZnTe/$CoTe_2$@NC/S, ZnTe/$CoTe_2$@NC/S, $CoTe_2$@NC/S, and $ZnTe_2$@NC/S composites. Upon sulfur incorporation, the structure of the host material was effectively inherited, with no sulfur aglomerates observed on the surface of the host material (**Figure S10-S12**). EELS chemical composition maps show S to be relatively evenly distributed across v-ZnTe/$CoTe_2$@NC/S (**Figure S13**). Compared to v-ZnTe/$CoTe_2$@NC (589 m^2 g^{-1}), upon the introduction of sulfur, a dramatic decrease in surface area was measured for v-ZnTe/$CoTe_2$@NC/S (32.9 m^2 g^{-1}), suggesting that S infiltrates throughout most of the host material pores (**Figure S14)**. Besides, X-ray powder diffraction (XRD) patterns further confirm the presence of S within the final electrode material (**Figure S15a)**. Thermogravimetry analysis (TGA) shows that the sulfur loading of v-ZnTe/$CoTe_2$@NC/S is about 68% (**Figure S15b**)

Coin cells were assembled using the sulfur cathodes, lithium foil as anode, and a solution of 1.0 M lithium bis(trifluoromethanesulfonyl)imide and 0.2 M $LiNO_3$ in a mixture of 1,3-dioxolane (DOL) and1,2-dimethoxyethane (DME) with a volume ratio of 1:1 as electrolyte (see details in the SI). The galvanostatic charge/discharge (GCD) curves of the different cathode materials (v-ZnTe/$CoTe_2$@NC/S, ZnTe/$CoTe_2$@NC/S, $CoTe_2$@NC/S, and ZnTe@NC/S) at a current rate 0.1C are shown in **Figure 4a and Table S2**. As generally observed in LSBs,[29] two distinct voltage plateaus are obtained during the cell discharge. The first voltage plateau at 2.4 ~ 2.1 V is mainly attributed to the conversion of S_8 to long-chain LiPSs (S_8 to Li_2S_4). The second voltage plateau in the voltage window of 2.1 ~ 1.7 V corresponds to the liquid-solid reaction of polysulfides gaining electrons and reducing to insoluble Li_2S_2 (Li_2S_4 to Li_2S_2) and the solid-solid reaction of Li_2S_2 to Li_2S. Compared with other sulfur cathodes, v-ZnTe/$CoTe_2$@NC/S exhibits the highest initial specific capacitance (1608 mAh g^{-1}), well above that of ZnTe/$CoTe_2$@NC/S (1290 mAh g^{-1}), $CoTe_2$@NC/S (1105 mAh g^{-1}) and ZnTe@NC/S (1005 mAh g^{-1}).

The GCD curves of the v-ZnTe/$CoTe_2$@NC/S, ZnTe/$CoTe_2$@NC/S, $CoTe_2$@NC/S, ZnTe@NC/S, and NC/S cathodes at various current rates are shown in **Figures 4b, S16 and S17.** As the current rate increased from 0.1C to 0.2C, 0.5C, 1C, 2C, and 3C, the specific capacitances of the v-ZnTe/$CoTe_2$@NC/S cathode decreased from 1608.8 to 1112.2, 908.9, 811.1, 698.7 and 618.2 mA h g^{-1}, respectively. A clear voltage plateau can be observed even at the highest current rate of 3C, indicating that the v-ZnTe/$CoTe_2$@NC host could effectively catalyze the conversion of LiPS. When the current rate returns to 0.2C, the specific capacity of the v-ZnTe/$CoTe_2$@NC/S electrode recovers to 1040 mAh g^{-1}, demonstrating notable

stability after high-rate charge-discharge processes. The performance of the v-ZnTe/$CoTe_2$@NC/S electrode was well above that of all the other electrodes, particularly ZnTe/$CoTe_2$@NC/S, demonstrating the positive effect played by the TMT catalyst, the Te vacancies and the heterojunctions.

The electrochemical performance of electrodes based on v-ZnTe/$CoTe_2$@NC composites annealed under Ar/H_2 for different times, thus containing different amounts of vacancies, is shown in **Figure S18.** We observe the electrode based on the composite annealed for just 1 h (v-ZnTe/$CoTe_2$@NC/S-1h) to be characterized by clearly lower specific capacities associated with a too-low content of Te vacancies. Besides, the electrode based on the composite annealed for 5 h (v-ZnTe/$CoTe_2$@NC/S-5h) also displayed a lower performance than that annealed for 3 h (v-ZnTe/$CoTe_2$@NC/S-1h). Thus, an optimum amount of Te vacancies exist. While too-short annealing times do not introduce enough Te vacancies, too-long times strongly reduce the material changing its electronic band structure and overall properties. Previous works have also shown the existence of an optimal vacancy concentration to maximize the performance of catalytic systems and energy storage devices [25, 30]

The voltage difference ΔE between the oxidation platform and the second reduction platform is generally regarded as the polarization potential of the Li-S reaction (**Figure 4c**).[7] The polarization voltage of the v-ZnTe/$CoTe_2$@NC (135 mV) electrode was significantly lower than that of ZnTe/$CoTe_2$@NC (144 mV), $CoTe_2$@NC (172 mV) and ZnTe@NC (184 mV). Thus while both heterostructured tellurides showed an effective promotion of the LiPSs reaction kinetics compared with the single tellurides, the presence of vacancies further enhanced the reaction kinetics.

The capacity ratio of the first discharge platform (Q_1) to the second discharge platform (Q_2) can be used as a quantitative representation of the catalytic activity of the host material for LiPS conversion.[1a] Since the first platform involves 4 electrons and the second platform involves 12 electrons of the full 16-electron S_8 lithiation process, the theoretical ratio of Q_2/Q_1 is 3. In practice, this ratio is always lower than 3 due to the dissolution of polysulfides that do not participate further in the reaction and the incomplete reduction from Li_2S_4 to Li_2S at the second discharge plateau. Thus Q_2/Q_1 values reflect the degree of completion of the reduction reaction, which is mainly related to the ability of the host material to catalyze it and inhibit the shuttling effect. The Q_2/Q_1 value of the four cathode materials (v-ZnTe/$CoTe_2$@NC/S, ZnTe/$CoTe_2$@NC/S, $CoTe_2$@NC/S, and ZnTe@NC/S) are shown in **Figure 4c**. Consistently with previous results, the v-ZnTe/$CoTe_2$@NC/S electrode exhibits the highest Q_2/Q_1 ratio at 2.82, close to the theoretical value and well above that of ZnTe/$CoTe_2$@NC (2.65), $CoTe_2$@NC (2.51) and ZnTe@NC (2.43). Again, the two heterostructured tellurides showed improved performance over the single tellurides and the presence of vacancies further boosted the catalytic performance of the heterostructured materials.

The rate performance curves of the different sulfur cathodes are shown in **Figure 4d-e**. The specific capacity of all electrodes gradually decreases with the increase of the current rate. The v-ZnTe/$CoTe_2$@NC/S electrode shows the highest specific capacities at all current rates, further demonstrating that the formation of vacancies and heterojunctions effectively promote polysulfide adsorption and charge transfer.

CV curves of the different cells at a scan rate of 0.1 mV^{-1} are shown in **Figure 4f**. All curves show two cathodic peaks (C_1 and C_2) and one anodic peak (A), which is consistent

with the measured charge/discharge plateaus. The two cathodic peaks and the anodic peak represent the reduction of sulfur to polysulfides ($S_8/Li_2S_8 \rightarrow Li_2S_6/Li_2S_4$) followed by their reduction to Li_2S_2/Li_2S ($Li_2S_6/Li_2S_4 \rightarrow Li_2S_2/Li_2S$), and the oxidation of polysulfides to sulfur ($Li_2S_2/Li_2S \rightarrow Li_2S_8/S_8$), respectively. Among the different cathode materials, v-ZnTe/$CoTe_2$@NC/S exhibits the highest current densities, showing the most effective conversion of polysulfides, and the lowest polarization voltages. The cathodic peaks of the v-ZnTe/$CoTe_2$@NC/S cathode show a much larger current density and are slightly shifted to higher potentials compared with the other cathodes, suggesting a promoted conversion of LiPSs to insoluble Li_2S_2/Li_2S within the v-ZnTe/$CoTe_2$@NC/S cathode. Besides, the oxidation peak of v-ZnTe/$CoTe_2$@NC/S is shifted to a lower potential, indicating an enhanced Li_2S decomposition.

The onset potentials at a current density of 10 μA cm^{-2} beyond the baseline current were used to quantitatively estimate the electrocatalytic activity (**Figures 4g and S 19**). Cells based on v-ZnTe/$CoTe_2$@NC/S cathodes showed the highest cathodic peak onset potentials and the lowest anodic peak onset potentials, which further demonstrated that the presence of vacancies and heterostructures accelerates the redox reaction kinetics.

CV curves at different scan rates, 0.1-0.4 mV s^{-1}, within a voltage window of 1.7-2.8 V were used to study the reaction kinetics and the lithium-ion diffusion (**Figure S20**). For all the cathode materials, as the scan rate increases, there is a gradual increase in the peak current intensity while the peak shape remains unaltered, which indicates excellent electrochemical properties. The CV curves show a linear relationship between the peak current (I_p) and the

square root of the scan rate (v), as shown in **Figures 4h and S21a-b**. According to the Randles-Sevcik equation:

$$I_p=2.69\text{x}10^5\ n^{1.5}A\ D_{Li}{}^{+0.5}C_{Li}{}^{+}\ v^{0.5}$$

Where n is the number of charges, A is the geometric area of the electrode, and $C_{Li}{}^{+}$ represents the concentration of Li^+. Thus, the diffusion coefficient of Li^+ (D_{Li}+) can be calculated from the linear fitting of I_p vs. $v^{0.5}$.

v-ZnTe/$CoTe_2$@NC/S electrodes displayed the sharpest slopes, corresponding to the highest $D_{Li}{}^{+}$ values at the two cathodic peaks and the anodic peak (taken as whole despite its broadness), 2.1 × 10^{-7}, 3.5 × 10^{-7}, and 5.7 × 10^{-7} cm^2 s^{-1}, respectively. The ZnTe/$CoTe_2$@NC/S electrode exhibited similar slopes and thus $D_{Li}{}^{+}$ values, which were well above those of $CoTe_2$@NC/S and ZnTe@NC/S (**Figure S21c**). These results indicate that the heterojunction accelerates the diffusion of Li^+ during the redox reaction, while vacancies played a minor role in this parameter.

To study the interfacial charge transfer kinetics, electrochemical impedance spectroscopy (EIS) measurements were performed. The Nyquist plots of the EIS spectra obtained from the v-ZnTe/$CoTe_2$@NC/S, ZnTe/$CoTe_2$@NC/S, $CoTe_2$@NC/S, and ZnTe@NC/S coin cells before and after cycling and the equivalent circuit are shown in **Figures 4i and S22-23**. All the electrodes show a semicircle in the high-frequency region related to the charge transfer resistance (R_{ct} in the equivalent circuit) and then a straight line in the low-frequency region whose slope is related to the Li-ion diffusion resistance.[31] In particular, the v-ZnTe/$CoTe_2$@NC/S fresh electrode showed the lowest R_{ct} (48.6 Ω) compared with ZnTe/$CoTe_2$@NC/S (61.8 Ω), $CoTe_2$@NC/S (88.6 Ω) and ZnTe@NC/S (97.6 Ω) electrodes.

Electrodes v-ZnTe/$CoTe_2$@NC/S and ZnTe/$CoTe_2$@NC/S show approximately equal slopes in the low-frequency region, but well larger than $CoTe_2$@NC/S and ZnTe@NC/S, indicating that the heterojunction facilitates the diffusion of Li^+, which is consistent with the Li^+diffusion coefficients calculated from the CV curves. After the charge-discharge cycle, an additional R-C element, i.e. an additional interphase, was required to fit the high-frequency range of the EIS spectra (R_p in the equivalent circuit). This additional element was related to the deposition of insulating discharge products of Li_2S on the electrode surface during the cycle. The v-ZnTe/$CoTe_2$@NC/S electrode showed considerably lower R_p and R_{ct} compared to ZnTe/$CoTe_2$@NC/S, $CoTe_2$@NC/S, and ZnTe@NC/S electrodes (**Figure S24**). These lower resistances are consistent with faster polysulfide conversion reactions and faster charge transfer kinetics during lithiation/delithiation reactions. A lower Rct was obtained after cycling associated with the chemical activation process of dissolution and redistribution of the active material.[32]

The cycle stability curves of the different electrodes (v-ZnTe/$CoTe_2$@NC/S, ZnTe/$CoTe_2$@NC/S, $CoTe_2$@NC/S, and ZnTe@NC/S) at a current rate of 1C for 500 cycles are shown in **Figure 4j**. The v-ZnTe/$CoTe_2$@NC/S-based cell exhibits the highest initial specific capacity, followed by the ZnTe/$CoTe_2$@NC/S. Besides, after 500 cycles, these two electrodes also showed the highest capacity retention at 82.5% and 56.7%, above that of $CoTe_2$@NC/S, and ZnTe@NC/S at 45.1%, and 25.6%, respectively (**Figure 4k**). These results are again consistent with the formation of vacancies and heterostructures favoring the conversion of polysulfides, preventing more polysulfides from dissolving into the electrolyte.

After 500 cycles, the coin cells were disassembled and analyzed (**Figure S25**). Compared with ZnTe/$CoTe_2$@NC/S, $CoTe_2$@NC/S, and ZnTe@NC/S, the membrane of v-ZnTe/$CoTe_2$@NC/S was almost transparent, indicating a lower amount of LiPS reaching the membrane. Besides, the lithium anode of the cycled v-ZnTe/$CoTe_2$@NC/S coin cell shows much lower corrosion (**Figure S26**) and a low concentration of S (**Figure S27**), further confirming the effective trapping of LiPs at this cathode.

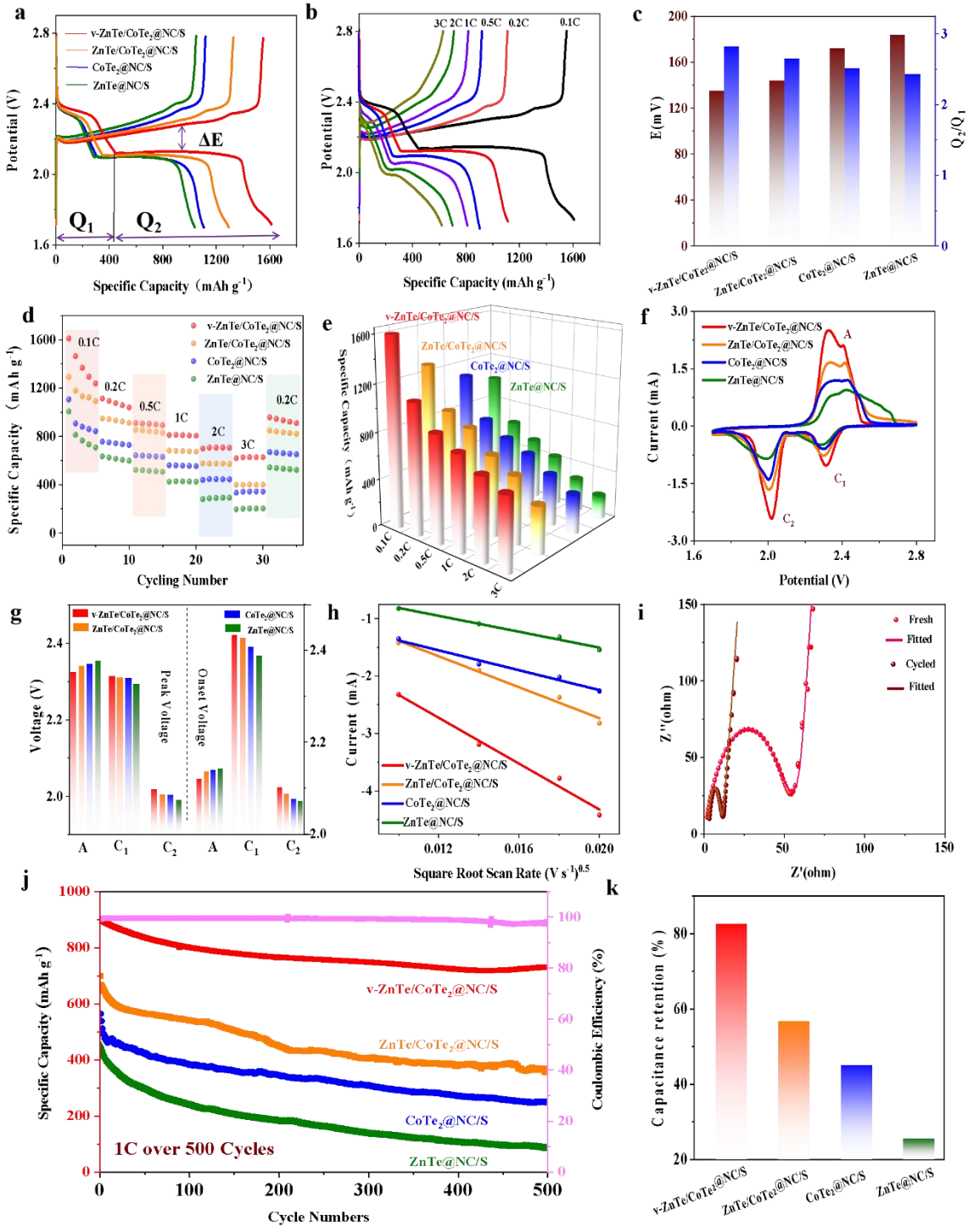

Figure 4. (a) GCD curves of the different cathodes (v-ZnTe/$CoTe_2$@NC/S, ZnTe/$CoTe_2$@NC/S, $CoTe_2$@NC/S, and ZnTe@NC/S) at a current rate of 0.1C. (b) GCD curve of v-ZnTe/$CoTe_2$@NC/S at a current density of 0.1C-3C. (c) ΔE and Q_2/Q_1 values of

the as-prepared electrode during the charge-discharge process. (d,e) Rate performance of the different electrodes. (f) CV curves of different electrodes at a scan rate of 0.1 mV^{-1}. (g) Peak and onset potentials of the different electrodes. (h) Peak current vs. square root curve of scan rate. (i) Nyquist plot of the EIS spectra of the v-ZnTe/$CoTe_2$@NC/S. (j) Long cycle test of different electrodes at 1C for 500 cycles and coulombic efficiency (v-ZnTe/$CoTe_2$@NC). (k) Capacitance retention after 500 cycles.

To determine the stability of the vacancies of the sulfur host material during cycling, the EPR spectrum of the cycled electrode material was analyzed and it is shown in **Figure S28**. A strong signal related to unpaired electrons and associated with the Te vacancies can be observed, showing that Te vacancies are maintained in the electrode material after cycling. However, the signal intensity decreased and its center position shifted from 2.003 to 1.98, which indicates the interaction of the Te vacancies with sulfur/polysulfides. Part of the original Te vacancies sites, particularly those at the material surface, may contain sulfur-based ions that the unpaired electrons thus not contributing to the EPR signal.

The performance dependence on the sulfur mass loading and the amount of electrolyte are important parameters to evaluate the practical application of LSB. The GCD curves of a high sulfur loading cell, 5.4 mg cm^{-1}, based on the v-ZnTe/$CoTe_2$@NC/S cathode are shown in **Figure 5a**. All the curves show a charging platform and two discharging platforms, denoting a proper performance. When the current rate is 0.1C, 0.2C, 0.5C, 1C, 2C, and 3C, the specific capacitances are 1273, 1104, 904.8, 808.3, 728.6, and 636.8 mA h g^{-1}, respectively (**Figure 5b**). When the current rate returns to 0.1C, the specific capacity of the v-ZnTe/$CoTe_2$@NC/S

electrode recovers to 1158 mAh g^{-1}. The moderate decrease in specific capacitance with the increasing current rate indicates that the v-ZnTe/$CoTe_2$@NC/S has an excellent rate performance even at this relatively high sulfur loading because of its better electron transfer properties.

At high sulfur loading (5.4 mg cm^{-2}), when the electrolyte amount was decreased to 12.3 μL mg^{-1}, the v-ZnTe/$CoTe_2$@NC/S cathode maintained a capacity above 1050 mAh g^{-1} for at least 100 cycles, which corresponds to a slow capacity fade of 0.18% per cycle (**Figure 5c**). When further reducing the electrolyte amount to 7.5 μL mg^{-1}, v-ZnTe/$CoTe_2$@NC/S still maintained a capacity of 890.8 mA h g^{-1} after 100 cycles (**Figure 5d**). These excellent results demonstrate that v-ZnTe/$CoTe_2$@NC effectively promotes the conversion of polysulfides, prevents the shuttling of polysulfides, and further improves the utilization of sulfur even at high loading and lean electrolyte conditions. By comparing with the other tested cathodes, this excellent performance must be associated with the formed heterostructures and the presence of tellurium vacancies. In addition, v-ZnTe/$CoTe_2$@NC/S cathodes stand out when compared with previous reports on sulfur host materials based on heterostructures or incorporating vacancies (**Figure S29 and Table S3,4**).[33]

Pouch cells based on v-ZnTe/$CoTe_2$@NC/S cathodes were further assembled and their cycle stability was tested (**Figure S30**). At a current rate of 0.1C, the pouch cells containing a sulfur loading of 5.6 mg cm^{-2} and 11.2 mL g^{-1} electrolyte retained 86.78% of their capacity after 150 cycles. **Figure 5e** displays how v-ZnTe/$CoTe_2$@NC/S-based pouch cells can power a temperature and humidity monitoring clock, showing that the prepared electrodes have practical applications. Additionally, the electrochemical performance of pouch cells with

higher sulfur loading and lower electrolyte composition were assembled and tested (**Figure S31)**. As observed in **Figure S31 a,c**, when the sulfur load was increased to 6.4 mg cm^{-2} and 8.2 mg cm^{-2}, the capacitance retention rates were 77.6% and 75.4% after 100 cycles at a current rate 3C. Besides, when reducing the electrolyte content to 6.3 mL g^{-1} and 4.8 mL g^{-1}, the capacitance retention rates were 85.9% and 83.3% after 100 cycles at a current rate 3C (**Figure S31 b,c**).

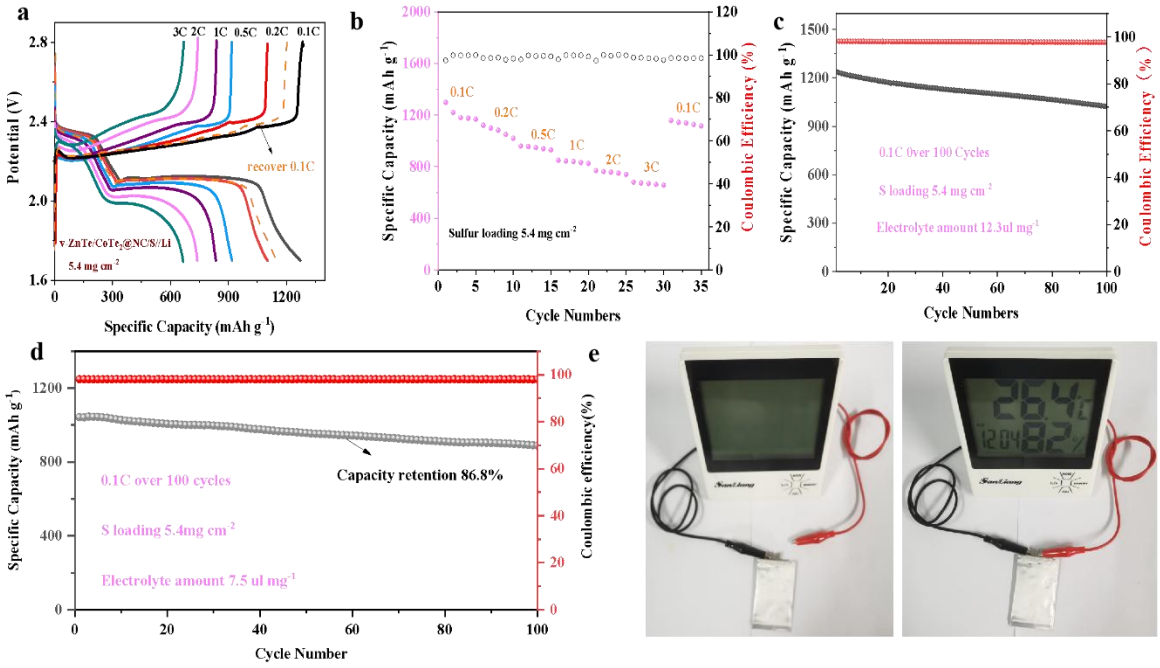

Figure 5. (a) GCD curve of electrode v-ZnTe/$CoTe_2$@NC/S under high loading (5.4 mg cm^{-2}). (b) Rate performance curve. (c-d) Cycling stability of v-ZnTe/$CoTe_2$@NC/S at 0.1C after 100 cycles at different electrolyte contents. (e) Two v-ZnTe/$CoTe_2$@NC/S-based pouch cells powering a commercial temperature and humidity monitoring clock.

3. Conclusions

In summary, a NC-based composite containing small amounts of ZnTe/$CoTe_2$ heterostructures with Te-vacancies as sulfur redox catalyst has been developed. As shown using both DFT calculations and experimental results, the presence of Te vacancies enhances the adsorption of LiPSs and promotes catalytic activity. The heterostructured TMT promotes the diffusion of ions and increases the electrical conductivity of the material. Benefiting from the optimized structure and composition, v-ZnTe/$CoTe_2$@NC/S exhibits high initial capacity (1608 mA h^{-1} at 0.1C), excellent rate capability, and long cycle life, even at high sulfur loading and in lean electrolyte conditions. Overall, this work demonstrates the combination of defect and interface engineering to be an effective strategy to optimize the electrochemical performance of LSB cathode materials.

Supporting information

Supporting Information is available from the Wiley Online Library or from the author.

Acknowledgements

The authors thank the support from the projects ENE2016-77798-C4-3-R and NANOGEN (PID2020-116093RB-C43), funded by MCIN/ AEI/10.13039/501100011033/ and by "ERDF A way of making Europe", by the "European Union". C.H., J.Y., C.H.Li, C.Q.Z., C.Y.Z. and B.F.N thank the China Scholarship Council for the scholarship support. ICN2 acknowledges the support from the Severo Ochoa Programme (MINECO, grant no. SEV-2017-0706). IREC and ICN2 are both funded by the CERCA Program/Generalitat de Catalunya. This project has received funding from the

European Union's Horizon 2020 research and innovation program under grant agreement No 823717-ESTEEM3.

Conflict of Interest

The authors declare no conflict of interest.

Data Availability Statement

The data that support the findings of this study are available from the corresponding author upon reasonable request.

References

[1] a) D. Yang, M. Li, X. Zheng, X. Han, C. Zhang, J. Jacas Biendicho, J. Llorca, J. Wang, H. Hao, J. Li, G. Henkelman, J. Arbiol, J. R. Morante, D. Mitlin, S. Chou, A. Cabot, *ACS Nano* **2022**, 16, 11102; b) R. Xiao, D. Luo, J. Wang, H. Lu, H. Ma, E. M. Akinoglu, M. Jin, X. Wang, Y. Zhang, Z. Chen, *Adv. Sci.* **2022**, 9, 2202352; c) W. Zhao, W. Zhang, Y. Lei, L. Wang, G. Wang, J. Wu, W. Fan, S. Huang, *ACS Appl. Mater. Interfaces* **2022**, 14, 6801.

[2] a) M. Li, D. Yang, J. J. Biendicho, X. Han, C. Zhang, K. Liu, J. Diao, J. Li, J. Wang, M. Heggen, R. E. Dunin-Borkowski, J. Wang, G. Henkelman, J. R. Morante, J. Arbiol, S.-L. Chou, A. Cabot, *Adv. Funct. Mater.* **2022**, 32, 2200529; b) B. Jiang, Y. Qiu, D. Tian, Y. Zhang, X. Song, C. Zhao, M. Wang, X. Sun, H. Huang, C. Zhao, H. Zhou, A. Chen, L. Fan, N. Zhang, *Adv. Energy Mater.* **2021**, 11, 2102995; c) E. Jung, S.-J. Kim, J. Kim, S. Koo, J. Lee, S.-Y. Kim, V. K. Paidi, W. Ko, J. Moon, K.-S. Lee, S.-P. Cho, D. Kim, S.-H. Yu, Y.-E. Sung, T. Hyeon, *ACS Energy Lett.* **2022**, 7, 2646.

[3] a) C. Wang, N. Sakai, Y. Ebina, T. Kikuchi, M. R. Snowdon, D. Tang, R. Ma, T. Sasaki, *J. Mater. Chem. A* **2021**, 9, 9952; b) X. Zhang, T. Yang, Y. Zhang, X. Wang, J. Wang, Y. Li, A. Yu, X. Wang, Z. Chen, *Adv. Mater.* **2023**, 35, 2208470; c) C. Y. Zhang, C. Zhang, G. W. Sun, J. L. Pan, L. Gong, G. Z.

Sun, J. J. Biendicho, L. Balcells, X. L. Fan, J. R. Morante, J. Y. Zhou, A. Cabot, *Angew. Chem.* **2022**, 61, e202211570; d) X. Sun, D. Tian, X. Song, B. Jiang, C. Zhao, Y. Zhang, L. Yang, L. Fan, X. Yin, N. Zhang, *Nano Energy* **2022**, 95, 106979.

[4] a) X. Lv, T. Lei, B. Wang, W. Chen, Y. Jiao, Y. Hu, Y. Yan, J. Huang, J. Chu, C. Yan, C. Wu, J. Wang, X. Niu, J. Xiong, *Adv. Energy Mater.* **2019**, 9, 1901800; b) Y. Gong, Y. Wang, Z. Fang, S. Zhao, Y.-s. He, W. Zhang, J. Mu, L. Zhang, Z.-F. Ma, *Chem. Eng. J.* **2022**, 446, 136943.

[5] a) S. Hu, M. Yi, H. Wu, T. Wang, X. Ma, X. Liu, J. Zhang, *Adv. Funct. Mater.* **2022**, 32, 2111084; b) D. Yang, Z. Liang, C. Zhang, J. J. Biendicho, M. Botifoll, M. C. Spadaro, Q. Chen, M. Li, A. Ramon, A. O. Moghaddam, J. Llorca, J. Wang, J. R. Morante, J. Arbiol, S.-L. Chou, A. Cabot, *Adv. Energy Mater.* **2021**, 11, 2101250; c) Z. Liang, D. Yang, P. Tang, C. Zhang, J. Jacas Biendicho, Y. Zhang, J. Llorca, X. Wang, J. Li, M. Heggen, J. David, R. E. Dunin-Borkowski, Y. Zhou, J. R. Morante, A. Cabot, J. Arbiol, *Adv. Energy Mater.* **2021**, 11, 2170022.

[6] a) L. Guan, H. Hu, L. Li, Y. Pan, Y. Zhu, Q. Li, H. Guo, K. Wang, Y. Huang, M. Zhang, Y. Yan, Z. Li, X. Teng, J. Yang, J. Xiao, Y. Zhang, X. Wang, M. Wu, *ACS Nano* **2020**, 14, 6222; b) J. Li, C. Chen, Y. Chen, Z. Li, W. Xie, X. Zhang, M. Shao, M. Wei, *Adv. Energy Mater.***2019**, 9, 1901935.

[7] J. Wang, Y. Zhao, G. Li, D. Luo, J. Liu, Y. Zhang, X. Wang, L. Shui, Z. Chen, *Nano Energy* **2021**, 84, 105891.

[8] C. Zhang, R. Du, S. Martí-Sánchez, K. Xiao, D. Yang, C. Zhang, C. Li, G. Zeng, X. Chang, R. He, J. Arbiol, J. Li, J. Jacas Biendicho, A. Cabot, in *Energies*, Vol. 16, 2023.

[9] a) D. Yang, Z. Liang, P. Tang, C. Zhang, M. Tang, Q. Li, J. J. Biendicho, J. Li, M. Heggen, R. E. Dunin-Borkowski, M. Xu, J. Llorca, J. Arbiol, J. R. Morante, S.-L. Chou, A. Cabot, *Adv. Mater.* **2022**,

34, 2108835; b) C. Zhang, B. Fei, D. Yang, H. Zhan, J. Wang, J. Diao, J. Li, G. Henkelman, D. Cai, J. J. Biendicho, J. R. Morante, A. Cabot, *Adv. Funct. Mater.* **2022**, 32, 2201322.

[10] a) R. Sun, Y. Bai, M. Luo, M. Qu, Z. Wang, W. Sun, K. Sun, *ACS Nano* **2021**, 15, 739; b) Y. Lu, J.-L. Qin, T. Shen, Y.-F. Yu, K. Chen, Y.-Z. Hu, J.-N. Liang, M.-X. Gong, J.-J. Zhang, D.-L. Wang, *Adv. Energy Mater.* **2021**, 11, 2101780; c) W. Zhao, Y. Lei, Y. Zhu, Q. Wang, F. Zhang, X. Dong, H. N. Alshareef, *Nano Energy* **2021**, 86, 106120; d) Z. Ye, Y. Jiang, L. Li, F. Wu, R. Chen, *Adv. Mater.* **2020**, 32, 2002168; e) T. Chen, Z. Zhang, B. Cheng, R. Chen, Y. Hu, L. Ma, G. Zhu, J. Liu, Z. Jin, *J.Am.Chem.Soc.* **2017**, 139, 12710; f) Y. Lu, J. L. Qin, T. Shen, Y. F. Yu, K. Chen, Y. Z. Hu, J. N. Liang, M. X. Gong, J. J. Zhang, D. L. Wang, *Adv. Energy Mater.* **2021**, 11.

[11] a) C. Xing, Y. Zhang, K. Xiao, X. Han, Y. Liu, B. Nan, M. G. Ramon, K. H. Lim, J. Li, J. Arbiol, B. Poudel, A. Nozariasbmarz, W. Li, M. Ibáñez, A. Cabot, *ACS Nano* **2023**, 17, 8442; b) W. Yao, C. Tian, C. Yang, J. Xu, Y. Meng, I. Manke, N. Chen, Z. Wu, L. Zhan, Y. Wang, R. Chen, *Adv. Mater.* **2022**, 34, 2106370.

[12] B. Wang, L. Wang, D. Ding, Y. Zhai, F. Wang, Z. Jing, X. Yang, Y. Kong, Y. Qian, L. Xu, *Adv. Mater.* **2022**, 34, 2204403.

[13] a) J.-Y. Xue, F.-L. Li, B. Chen, H. Geng, W. Zhang, W.-Y. Xu, H. Gu, P. Braunstein, J.-P. Lang, *Appl. Catal. B Environ.* **2022**, 312, 121434; b) L. Jiang, J. Duan, J. Zhu, S. Chen, M. Antonietti, *ACS Nano* **2020**, 14, 2436; c) X. Wang, X. Han, R. Du, C. Xing, X. Qi, Z. Liang, P. Guardia, J. Arbiol, A. Cabot, J. Li, *ACS Appl. Mater. Interfaces* **2022**, 14, 41924; d) R. Du, K. Xiao, B. Li, X. Han, C. Zhang, X. Wang, Y. Zuo, P. Guardia, J. Li, J. Chen, J. Arbiol, A. Cabot, *Chem. Eng. J.* **2022**, 441, 135999.

[14] a) L. Zhang, J. Bi, T. Liu, X. Chu, H. Lv, D. Mu, B. Wu, F. Wu, *Energy Storage Mater.* **2023**, 54, 410; b) J. Wang, B. Wang, H. Sun, G. Wang, J. Bai, H. Wang, *Energy Storage Mater.* **2022**, 46, 394.

[15] a) J.-Y. Xue, F.-L. Li, B. Chen, H. Geng, W. Zhang, W.-Y. Xu, H. Gu, P. Braunstein, J.-P. Lang, *Appl.Catal B* **2022**, 312; b) S. R. K. A, N. Barman, S. Radhakrishnan, R. Thapa, C. S. Rout, *J. Mater. Chem. A* **2022**, 10, 23590; c) L. Luo, X. Wang, S. Yang, J. Dai, D. Li, L. Xia, C. Chi, A. Cabot, Y. Xu, L. Dai, *ACS Appl. Energy Mater.* **2023**, 6, 5940; d) J. Dai, X. Qi, L. Xia, Q. Xue, L. Luo, X. Wang, C. Yang, D. Li, H. Xie, A. Cabot, L. Dai, Y. Xu, *Adv. Funct. Mater.* **2023**, 33, 2212440.

[16] Y. Li, J. Zhang, Q. Chen, X. Xia, M. Chen, *Adv. Mater.* **2021**, 33, 2100855.

[17] M. Zhang, J. Mu, Y. Li, Y. Pan, Z. Dong, B. Chen, S. Guo, W. Yuan, H. Fang, H. Hu, M. Wu, *J. Energy Chem.* **2023**, 78, 105.

[18] Y. Zhang, C. Xing, Y. Liu, M. C. Spadaro, X. Wang, M. Li, K. Xiao, T. Zhang, P. Guardia, K. H. Lim, A. O. Moghaddam, J. Llorca, J. Arbiol, M. Ibáñez, A. Cabot, *Nano Energy* **2021**, 85, 105991.

[19] a) S. Hu, X. Huang, L. Zhang, G. Li, S. Chen, J. Zhang, X. Liu, *Adv. Funct. Mater.* **2023**, n/a, 2214161; b) W. Li, Y. Ma, P. Li, X. Jing, K. Jiang, D. Wang, *Adv. Energy Mater.* **2021**, 11, 2102607; c) W. Hou, P. Feng, X. Guo, Z. Wang, Z. Bai, Y. Bai, G. Wang, K. Sun, *Adv. Mater.* **2022**, 34, 2202222.

[20] S. Hu, X. Huang, L. Zhang, G. Li, S. Chen, J. Zhang, X. Liu, *Adv. Funct. Mater.* **2023**, 33, 2214161.

[21] a) D. Yang, C. Zhang, J. J. Biendicho, X. Han, Z. Liang, R. Du, M. Li, J. Li, J. Arbiol, J. Llorca, Y. Zhou, J. R. Morante, A. Cabot, *ACS Nano* **2020**, 14, 15492; b) X. Wang, X. Han, R. Du, Z. Liang, Y. Zuo, P. Guardia, J. Li, J. Llorca, J. Arbiol, R. Zheng, A. Cabot, *Appl. Catal. B* **2023**, 320, 121988.

[22] a) S. Liu, Z. Wang, S. Zhou, F. Yu, M. Yu, C.-Y. Chiang, W. Zhou, J. Zhao, J. Qiu, *Adv. Mater.***2017**, 29, 1700874; b) X. Wang, J. Li, Q. Xue, X. Han, C. Xing, Z. Liang, P. Guardia, Y. Zuo, R. Du, L. Balcells, J. Arbiol, J. Llorca, X. Qi, A. Cabot, *ACS Nano* **2023**, 17, 825.

[23] a) X. Wang, C. Xing, Z. Liang, P. Guardia, X. Han, Y. Zuo, J. Llorca, J. Arbiol, J. Li, A. Cabot, *J. Mater. Chem. A* **2022**, 10, 3659; b) C. Fu, X. Qi, L. Zhao, T. Yang, Q. Xue, Z. Zhu, P. Xiong, J. Jiang,

X. An, H. Chen, J. S. Chen, A. Cabot, R. Wu, *Appl. Catal. B* **2023**, 335, 122875; c) X. Wang, L. Yang, C. Xing, X. Han, R. Du, R. He, P. Guardia, J. Arbiol, A. Cabot, in *Nanomaterials*, Vol. 12, 2022.

[24] Y. Jiang, F. Wu, Z. Ye, Y. Zhou, Y. Chen, Y. Zhang, Z. lv, L. Li, M. Xie, R. Chen, *Chem. Eng. J.* **2023**, 451, 138430.

[25] C. Huang, A. Gao, F. Yi, Y. Wang, D. Shu, Y. Liang, Z. Zhu, J. Ling, J. Hao, *Chem. Eng. J.* **2021**, 419, 129643.

[26] C. Zhang, H. Li, X. Zeng, S *Chem. Eng. J.*. Xi, R. Wang, L. Zhang, G. Liang, K. Davey, Y. Liu, L. Zhang, S. Zhang, Z. Guo, *Adv. Energy Mater.* **2022**, 12, 2202577.

[27] W. Bao, L. Liu, C. Wang, S. Choi, D. Wang, G. Wang, *Adv. Energy Mater.* **2018**, 8, 1702485.

[28] S. Feng, Z.-H. Fu, X. Chen, Q. Zhang, *InfoMat* **2022**, 4, e12304.

[29] R. Zou, W. Liu, F. Ran, *InfoMat* **2022**, 4, e12319.

[30] a) D. Yan, W. Wang, X. Luo, C. Chen, Y. Zeng, Z. Zhu, *Chem. Eng. J.* **2018**, 334, 864; b) F. Lu, M. Zhou, W. Li, Q. Weng, C. Li, Y. Xue, X. Jiang, X. Zeng, Y. Bando, D. Golberg, *Nano Energy* **2016**, 26, 313.

[31] C. Zhang, J. J. Biendicho, T. Zhang, R. Du, J. Li, X. Yang, J. Arbiol, Y. Zhou, J. R. Morante, A. Cabot, *Adv. Funct. Mater.* **2019**, 29, 1903842.

[32] C. Zhang, R. Du, J. J. Biendicho, M. Yi, K. Xiao, D. Yang, T. Zhang, X. Wang, J. Arbiol, J. Llorca, Y. Zhou, J. R. Morante, A. Cabot, *Adv. Energy Mater.* **2021**, 11.

[33] a) H.-J. Li, K. Xi, W. Wang, S. Liu, G.-R. Li, X.-P. Gao, *Energy Storage Mater.* **2022**, 45, 1229; b) H. Song, T. Li, T. He, Z. Wang, D. Fang, Y. Wang, X. L. Li, D. Zhang, J. Hu, S. Huang, *Chem. Eng. J.* **2022**, 450, 138115; c) G. Liu, Q. Zeng, Z. Fan, S. Tian, X. Li, X. Lv, W. Zhang, K. Tao, E. Xie, Z. Zhang, *Chem. Eng. J.* **2022**, 448, 137683; d) L. Wu, J. Hu, X. Yang, Z. Liang, S. Chen, L. Liu, H. Hou,

J. Yang, *J. Mater. Chem. A* **2022**, 10, 23811; e) Z. Wu, S. Chen, L. Wang, Q. Deng, Z. Zeng, J. Wang, S. Deng, *Energy Storage Mater.* **2021**, 38, 381; f) D. Cai, B. Liu, D. Zhu, D. Chen, M. Lu, J. Cao, Y. Wang, W. Huang, Y. Shao, H. Tu, W. Han, *Adv. Energy Mater.* **2020**, 10, 2070088; g) S. Zhao, X. Tian, Y. Zhou, B. Ma, A. Natarajan, *J.Energy Chem.* **2020**, 46, 22; h) S. Chen, J. Luo, N. Li, X. Han, J. Wang, Q. Deng, Z. Zeng, S. Deng, *Energy Storage Mater.* **2020**, 30, 187.

Chen Huang, Jing Yu, Canhuang Li, Zhibiao Cui, Chaoqi Zhang, Chaoyue Zhang*, Bingfei Nan, Junshan Li, Jordi Arbiol, and Andreu Cabot**

Combined Defect and Heterojunction Engineering in ZnTe/$CoTe_2$@NC Sulfur Hosts toward Robust Lithium-Sulfur Batteries

The present study employs a dual engineering approach, manipulating vacancies and heterointerfaces, to develop an optimized transition metal tellurides (TMTs) catalytic additive. More precisely, N-doped carbon-coated bimetallic telluride heterostructures containing Te vacancies (v-ZnTe/$CoTe_2$@NC) are used as sulfur hosts in Lithium-sulfur battery. The exceptional electrochemical performance of v-ZnTe/$CoTe_2$@NC as sulfur host, which can be attributed to the synergistic effects and functionality of vacancies and heterointerface.

ToC figure